

Nonlinear microwave photon-occupancy of a driven resonator strongly coupled to a transmon qubit

B. Suri,^{1,2,*} Z. K. Keane,³ Lev S. Bishop,⁴ S. Novikov,^{1,2} F. C. Wellstood,^{2,5,6} and B. S. Palmer^{1,2}

¹*Laboratory for Physical Sciences, College Park, MD 20740, USA*

²*Department of Physics, University of Maryland, College Park, MD 20742, USA*

³*Northrop Grumman Electronic Systems, Linthicum, MD 21090, USA*

⁴*IBM T.J. Watson Research Center, Yorktown Heights, NY 10598, USA*

⁵*Joint Quantum Institute, University of Maryland, College Park, MD 20742, USA*

⁶*Center for Nanophysics and Advanced Materials,
University of Maryland, College Park, MD 20742, USA*

We measure photon-occupancy in a thin-film superconducting lumped element resonator coupled to a transmon qubit at 20 mK and find a nonlinear dependence on the applied microwave power. The transmon-resonator system was operated in the strong dispersive regime, where the ac Stark shift (2χ) due to a single microwave photon present in the resonator was larger than the linewidth (Γ) of the qubit transition. When the resonator was coherently driven at 5.474325 GHz, the transition spectrum of the transmon at 4.982 GHz revealed well-resolved peaks, each corresponding to an individual photon number-state of the resonator. From the relative peak-heights we obtain the occupancy of the photon-states and the average photon-occupancy \bar{n} of the resonator. We observed a nonlinear variation of \bar{n} with the applied drive power P_{rf} for $\bar{n} < 5$ and compare our results to numerical simulations of the system-bath master equation in the steady state, as well as to a semi-classical model for the resonator that includes the Jaynes-Cummings interaction between the transmon and the resonator. We find good quantitative agreement using both models and analysis reveals that the nonlinear behavior is principally due to shifts in the resonant frequency caused by a qubit-induced Jaynes-Cummings nonlinearity.

I. INTRODUCTION

Many interesting quantum effects in superconducting circuits are fundamentally due to the nonlinearity of the Josephson junction. For a transmon [1], which is just a capacitively shunted Josephson junction with carefully chosen parameters, the junction causes sufficient anharmonicity in the energy eigenstates so that the two lowest levels can be isolated as a qubit. When this artificial ‘atom’ couples strongly to the electromagnetic field of a resonator [2, 3] the same nonlinearity results in a variety of circuit QED (cQED) effects including photon number-splitting [4–6], nonclassical photonic states [7–10] and the Autler-Townes effect [6, 11, 12].

Understanding of the nonlinear effects produced by the Josephson junction has also enabled improved qubit read-out [13, 14] and the development of quantum-limited parametric amplifiers [15, 16]. The use of qubit readout techniques based on cQED effects is now widespread in quantum computing research. While most experimental efforts have been focused on using the techniques to examine qubits, the nonlinear quantum effects underlying such techniques are also of considerable interest.

In this article, we examine nonlinear effects in the simplest cQED system, a resonator that is strongly coupled to a transmon. In particular, we study the nonlinear dependence of the average stored photon-number \bar{n} in the resonator, versus the applied microwave power P_{rf} . When the coupling between the transmon and the resonator is large enough, the ac-Stark shift due to a single photon stored in the cavity can shift the qubit frequency by more than a spectral line-width resulting in “photon number-

* surib@chalmers.se; Present address: Department of Microtechnology and Nanoscience, Chalmers University of Technology, 41296-Gothenburg, Sweden.

splitting” of the qubit spectrum [5, 6]. The photon occupancy \bar{n} in the resonator can be directly found by measuring the transmon spectrum. Gambetta *et al.* [4] predicted a nonlinear relationship between \bar{n} and P_{rf} due to the Jaynes-Cummings interaction between the qubit and the resonator. Here we provide a detailed experimental examination of this effect in the small \bar{n} limit. We also compare our results to numerical simulations of the system-bath master equation in the steady state, as well as a semi-classical model for the resonator that includes the Jaynes-Cummings interaction between the transmon and the resonator, and find good quantitative agreement using both models.

In the following section, we first discuss the theory of the driven transmon-resonator system using the Jaynes-Cummings Hamiltonian in the

dispersive approximation and identify the leading nonlinear terms. We then set up a master equation to model losses and decoherence. In section III we describe the experimental set-up used for the experiment and discuss the measured system parameters in section IV. In section V we examine our results and compare them with the simulations, and then conclude in section VI with a summary and brief remarks on nonlinear qubit read-out techniques.

II. DRIVEN JAYNES-CUMMINGS SYSTEM

Coupling of a transmon to the electromagnetic field in a microwave resonator can be modeled using a generalized Jaynes-Cummings Hamiltonian [17, 18]:

$$H_{JC} = \hbar\omega_r a^\dagger a + \sum_{j=\{g,e,f,\dots\}} \hbar\omega_j |j\rangle\langle j| + \sum_{j=\{g,e,f,\dots\}} \hbar g_{j,j+1} \{a^\dagger |j\rangle\langle j+1| + a |j+1\rangle\langle j|\} . \quad (1)$$

Here ω_r is the bare resonator frequency, a^\dagger (a) is the creation (annihilation) operator for the resonator mode, the transmon states $|j\rangle$ are labelled $\{g, e, f, \dots\}$, and $g_{j,j+1}$ is the coupling strength of the $|j\rangle \leftrightarrow |j+1\rangle$ transition of the transmon with the resonator mode. In this form, the Josephson nonlinearity resides in the anharmonicity of the ω_j .

The coupling term containing $g_{j,j+1}$ in Eq. 1 is the Jaynes-Cummings interaction (see Fig. 1(a)) and it gives a block-diagonal structure to the Hamiltonian. In particular, for an m -level system coupled to a resonator, the

n -excitation manifold is spanned by m states $\{|0, n\rangle, |1, n-1\rangle, \dots, |m-1, n-m+1\rangle\}$. The corresponding $m \times m$ block matrix can then be diagonalized exactly for small m (numerically for large m) to compute the eigenenergies of the coupled system.

The Hamiltonian can also be approximately diagonalized in the dispersive limit [19, 20] corresponding to $\Delta_{j,j+1} \equiv \omega_{j,j+1} - \omega_r \gg g_{j,j+1}$, where $\omega_{j,j+1} \equiv \omega_{j+1} - \omega_j$ is the frequency of the $|j\rangle \leftrightarrow |j+1\rangle$ transmon transition. To diagonalize H_{JC} , we make a unitary transformation using:

$$\mathcal{T} = \exp \left(\sum_{j=\{g,e,f,\dots\}} \lambda_{j,j+1} \{a |j+1\rangle\langle j| - a^\dagger |j\rangle\langle j+1|\} \right) , \quad (2)$$

where $\lambda_{j,j+1} \equiv g_{j,j+1}/\Delta_{j,j+1} \ll 1$ is the small parameter in which a perturbative expansion of

the transformation can be carried out.

Truncating the resulting transformed Hamiltonian to the two lowest transmon levels, H_{JC} can be written in the qubit approximation up to fourth order in $\lambda_{j,j+1}$ as [17]:

$$\begin{aligned} \mathcal{T}H_{JC}\mathcal{T}^\dagger \approx H_{JC}^{(4)} \approx & \hbar\tilde{\omega}_r a^\dagger a + \hbar\frac{\tilde{\omega}_{ge}}{2}\sigma_z \\ & + \hbar\chi a^\dagger a \sigma_z + \hbar\zeta(a^\dagger a)^2\sigma_z + \hbar\zeta'(a^\dagger a)^2, \end{aligned} \quad (3)$$

where σ_z is the Pauli spin-matrix operating on the transmon $|g\rangle$ and $|e\rangle$ states, $\tilde{\omega}_r \equiv \omega_r - \chi_{ef}/2$ is the Lamb-shifted resonator frequency, $\tilde{\omega}_{ge} \equiv \omega_{ge} + \chi_{ge}$ is the Lamb-shifted qubit frequency, and $\chi_{ge} = g_{ge}^2/\Delta_{ge}$ and $\chi_{ef} = g_{ef}^2/\Delta_{ef}$ are the dispersive shifts of the resonator due to the transmon $|g\rangle \rightarrow |e\rangle$ and $|e\rangle \rightarrow |f\rangle$ transitions respectively. In this approximation the total qubit state-dependent dispersive shift of the resonator frequency is given by $\chi \simeq \chi_{ge} - \chi_{ef}/2$ [19]. Thus Eq. 3 includes perturbative shifts to the energy levels of the system due to the second-excited transmon state $|f\rangle$ [21] although this state itself is not explicitly included in Eq. 3. We note that the anharmonicity was sufficiently large compared to the strength of the drive tones in our experiment that transitions to $|f\rangle$ were negligible.

The term $\hbar\chi a^\dagger a \sigma_z$ in Eq. 3 represents an ac-Stark shift [19] of the qubit transition frequency by an amount 2χ for every photon in the cavity (see Fig. 1(b)). We note that Eq. 3 also has two fourth order terms that generate a Kerr-type nonlinearity. The resonator-qubit cross-Kerr coefficient ζ and the resonator self-Kerr coefficient ζ' [4, 17] are determined from:

$$\begin{aligned} \zeta \approx & \chi_{ef}\lambda_{ef}^2 - 2\chi_{ge}\lambda_{ge}^2 \\ & + \frac{7\chi_{ef}}{4}\lambda_{ge}^2 - \frac{5\chi_{ge}}{4}\lambda_{ef}^2 \end{aligned} \quad (4)$$

$$\zeta' \approx (\chi_{ge} - \chi_{ef})(\lambda_{ge}^2 + \lambda_{ef}^2). \quad (5)$$

From Eq. 3, the resonant frequency ω_r of the resonator can be seen to depend on the photon number $n = a^\dagger a$ according to

$$\omega_r(n) = \tilde{\omega}_r + \chi\sigma_z + \zeta n\sigma_z + \zeta'n. \quad (6)$$

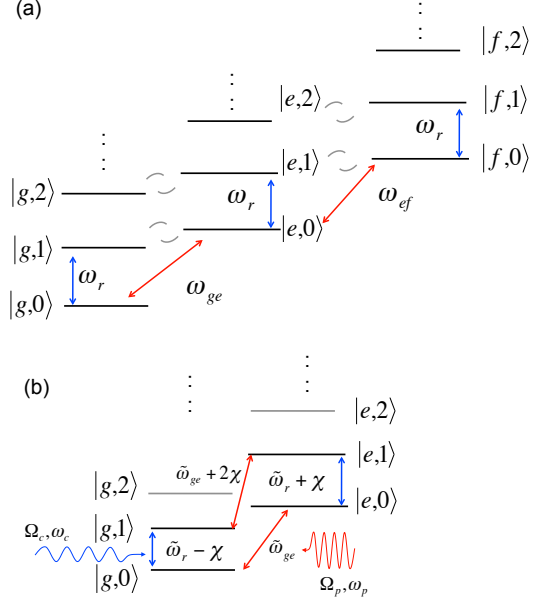


FIG. 1. (Color online) (a) Energy levels of the uncoupled transmon-resonator Jaynes-Cummings Hamiltonian for $m = 3$ transmon levels (g, e, f). (b) Energy levels after diagonalization in the dispersively coupled qubit approximation. The blue (red) wavy arrow denotes coupler (probe) drive field with strength $\Omega_{c(p)}$ and frequency $\omega_{c(p)}$.

We note that the n -dependence of the resonant frequency ω_r arises solely from the Kerr-type nonlinear terms up to this order of the approximate Hamiltonian. Thus the Kerr terms represent the lowest order approximation of the full nonlinearity arising from the Jaynes-Cummings interaction. It is this Kerr-type shift that causes the nonlinear dependence of the average photon-occupancy of the resonator \bar{n} discussed in section V.

In our experiment, we drive the transmon and the resonator using a “probe” tone and “coupler” tone respectively. We model the drives

using the Hamiltonian

$$H_d(t) = -\frac{\hbar\Omega_c}{2}(ae^{i\omega_c t} + a^\dagger e^{-i\omega_c t}) - \frac{\hbar\Omega_p}{2}(\sigma^- e^{i\omega_p t} + \sigma^+ e^{-i\omega_p t}), \quad (7)$$

where ω_c (ω_p) is the frequency of the coupler (probe) tone, Ω_c (Ω_p) is the amplitude of the coupler (probe) tone driving the resonator (qubit), and σ^+ and σ^- are the raising and lowering operators for the qubit. The Hamiltonian H_d is written in the rotating wave approximation in the limit of weak driving ($\Omega_{c(p)} \ll \omega_{c(p)}$) [19]. For simplicity, we also ignore terms of order $\lambda_{j,j+1}^2$ in H_d that arise from the dispersive transformation \mathcal{T} . The driven Jaynes-Cummings Hamiltonian in the dispersive approximation can then be written as

$$H \simeq H_{JC}^{(4)} + H_d(t) \quad (8)$$

To remove the explicit time-dependence in Eq. 8 we transform into a frame rotating with the drives, using a unitary transformation [19, 21] given by

$$U = e^{i\omega_c(a^\dagger a)t + i\omega_p\sigma_z t/2}. \quad (9)$$

The transformed time-independent Hamiltonian can be written as

$$H_I = U H U^\dagger + i\hbar\dot{U}U^\dagger \quad (10)$$

which gives

$$H_I/\hbar = \tilde{\Delta}_c a^\dagger a + \frac{\tilde{\Delta}_p}{2}\sigma_z + \chi(a^\dagger a)\sigma_z + \zeta(a^\dagger a)^2\sigma_z + \zeta'(a^\dagger a)^2 - \frac{\Omega_c}{2}(a + a^\dagger) - \frac{\Omega_p}{2}(\sigma^- + \sigma^+) \quad (11)$$

where $\tilde{\Delta}_c \equiv \omega_r - \omega_c$ and $\tilde{\Delta}_p \equiv \tilde{\omega}_{ge} - \omega_p$.

To include dissipation in the model we assume the transmon-resonator system is coupled to a thermal reservoir at temperature T . We write the master equation for the system density

matrix ρ in the Born-Markovian approximation [19, 22] as

$$\dot{\rho} = -\frac{i}{\hbar}[H, \rho] + \kappa_- \mathcal{D}[a]\rho + \kappa_+ \mathcal{D}[a^\dagger]\rho + \Gamma_- \mathcal{D}[\sigma^-]\rho + \Gamma_+ \mathcal{D}[\sigma^+]\rho + \frac{\gamma_\varphi}{2} \mathcal{D}[\sigma_z]\rho \quad (12)$$

where $\mathcal{D}[A_i]\rho \equiv A_i \rho A_i^\dagger - \frac{1}{2}(A_i^\dagger A_i \rho + \rho A_i^\dagger A_i)$, H is given by Eq. 8, γ_φ is the qubit dephasing-rate, κ_- is the resonator photon loss-rate and κ_+ is the photon excitation-rate. Similarly, for the qubit, the relaxation rate is given by Γ_- and the excitation rate by Γ_+ . The loss-rate and excitation rate are related by a Boltzmann factor according to $\kappa_+/\kappa_- \simeq e^{-\hbar\omega_r/k_B T}$ for the resonator, and $\Gamma_+/\Gamma_- \simeq e^{-\hbar\omega_{ge}/k_B T}$ for the transmon [23]. The explicit time-dependence in H can be removed by transforming Eq. 12 using the operator U in Eq. 9 to get

$$\dot{\rho} = -\frac{i}{\hbar}[H_I, \rho] + \kappa_- \mathcal{D}[a]\rho + \kappa_+ \mathcal{D}[a^\dagger]\rho + \Gamma_- \mathcal{D}[\sigma^-]\rho + \Gamma_+ \mathcal{D}[\sigma^+]\rho + \frac{\gamma_\varphi}{2} \mathcal{D}[\sigma_z]\rho. \quad (13)$$

The steady state condition $\dot{\rho} = 0$ reduces this master equation to a set of coupled linear equations in the elements of the density matrix ρ . After truncating the number of photon levels, typically to around fifteen, the resulting equations were numerically solved [25] to compare to the experimental results (see Sec. V).

III. EXPERIMENT

Figure 2 shows a colorized micrograph of our transmon (red) coupled to a superconducting lumped-element resonator (blue) [24, 25]. The device was patterned using photolithography and electron-beam lithography and was made of thin-film aluminum on a sapphire substrate. The resonator is formed from a meandering inductor and an interdigitated capacitor with a bare resonator frequency $\omega_r/2\pi = 5.464$ GHz. The resonator is coupled to an input/output coplanar waveguide transmission line (purple) which is used to excite and measure the system.

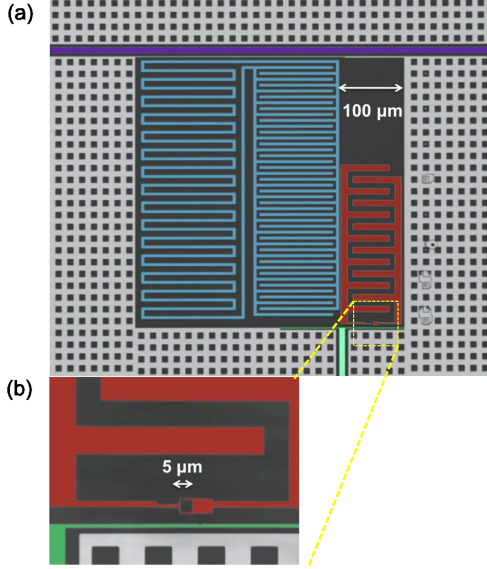


FIG. 2. (Color online) (a) Colorized micrograph of the device [25]. A lumped element resonator (blue) and transmon (red) are coupled to a coplanar waveguide transmission line (violet) and surrounded by a perforated ground plane (gray). The resonator consists of a meandering inductor and interdigitated capacitor. The transmon has two Josephson junctions in parallel to allow tuning of the transition frequency using an external magnetic field and on-chip flux bias line (green). (b) Detailed view of Josephson junctions and flux bias line.

The transmon [1] is formed from two Al/AlO_x/Al Josephson junctions that are shunted by an interdigitated capacitor with 13 fingers. Each finger has a width of 10 μm, a length of 70 μm, and is separated from adjacent fingers by 10 μm, using e-beam lithography. The junctions, each of area $\approx 100 \times 100 \text{ nm}^2$, were formed by double-angle evaporation [25, 26]. They are connected to form a

superconducting loop of area $4 \times 4.5 \mu\text{m}^2$ and the loop is placed close to a shorted current bias line (green region in Fig. 2). This arrangement allows us to apply flux to the loop to finely tune the critical current of the parallel junctions and hence the transition frequency of the qubit. The normal-state resistance of the two Josephson junctions in parallel yielded a maximum Josephson energy $E_{J,max}/h \approx 25 \text{ GHz}$ and the transmon had a Coulomb charging energy of $E_c/h = 250 \text{ MHz}$. This gave a maximum ground-to-first excited state transition frequency $\omega_{ge,max}/2\pi \simeq (\sqrt{8E_{J,max}E_c} - E_c)/h = 7.1 \text{ GHz}$ for the qubit.

The device was mounted in a hermetically sealed copper box and attached to the mixing chamber of an Oxford Kelvinox 100 dilution refrigerator with a base temperature of 20 mK. To isolate the device from thermal noise at higher temperatures, the input microwave line to the device had a 10 dB attenuator (Midwest microwave) mounted at 4 K, 20 dB at 0.7 K, and 30 dB at 20 mK on the mixing chamber, for a nominal total attenuation of 60 dB. On the output microwave line, two 18 dB isolators (Pantech) with bandwidths from 4 to 8 GHz were placed in series at 20 mK, followed by a 3 dB attenuator and a high electron mobility transistor (HEMT) amplifier (Caltech 4-8 GHz bandwidth, 40 dB gain) at 4 K.

To observe the photon-number-split spectrum, three microwave tones were applied on the input line to the device: probe, coupler, and read-out (see Fig. 3). The read-out and probe tones were pulsed on and off, while the coupler tone was applied continuously for the duration of the measurement. We used the high-power nonlinear Jaynes-Cummings read-out technique [14, 17, 21] to measure the excited state probability of the transmon. A probe pulse was first applied for a duration of 5 μs at an amplitude just large enough to saturate the qubit transition without causing large power broadening. We then waited 20 ns and applied a read-out pulse for 5 μs at a high power (*i.e.* 50 dB larger than the power of the coupler tone) at the bare resonator frequency ω_r . In our experiment, when the transmon is in the $|g\rangle$ state a

IV. SYSTEM PARAMETERS

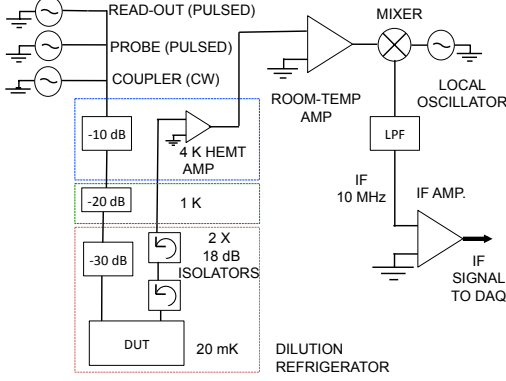


FIG. 3. (Color online) Schematic of the measurement set-up used for the number-splitting measurements.

We determined the main system parameters from spectroscopic and time-domain measurements. The resonator parameters were characterized by measuring the microwave transmission close to the resonant frequency as a function of input microwave power (data not shown). We measured a “bare” resonant frequency $\omega_r/2\pi = 5.464$ GHz at large input powers. At small input powers, a “dressed” resonant frequency of $(\tilde{\omega}_r - \chi)/2\pi = (\omega_r - \chi_{ge})/2\pi = 5.474325$ GHz was measured with the qubit in the ground state. We also measured an internal quality factor $Q_I = 190,000$, an external coupling quality factor $Q_e = 20,000$ and a loaded quality factor $Q_L \equiv \omega_r/\kappa_- = 18,000$ corresponding to a $\kappa_- = 2\pi(300)$ kHz.

The qubit transition frequency was tuned to $\tilde{\omega}_{ge}/2\pi = 4.982$ GHz using a combination of an external superconducting magnet and the on-chip flux bias, corresponding to a detuning of $\Delta_{ge}/2\pi = -482$ MHz from the bare resonator frequency. The effective dispersive shift $\chi/2\pi = -4.65$ MHz was determined from the difference in the frequencies of the $n = 0$ and $n = 1$ qubit spectral peaks (see Fig. 4(a)). From this we found $g_{ge}/2\pi = 70$ MHz, $\chi_{ge}/2\pi = -10.3$ MHz, $\chi_{ef}/2\pi = -10.7$ MHz and $g_{ef}/2\pi = 89$ MHz. The Kerr coefficients $\zeta/2\pi = 85$ kHz and $\zeta' = -23$ kHz were then calculated using Eq. 4 and Eq. 5 respectively [6, 25].

large transmissivity (S_{21}) of the read-out tone is observed and when the transmon is in an excited state ($|e\rangle$, $|f\rangle$ etc.) a small transmissivity is observed. The output read-out microwave signal was amplified again (Miteq 4-8 GHz, 30 dB gain) at room temperature and mixed down to an intermediate frequency (IF) of 10 MHz (see Fig. 3). The IF signal along with a phase reference was digitized at 1 GSa/s [25] using a data acquisition card and the in-phase and quadrature components were demodulated before being recorded.

Time-domain coherence measurements revealed a qubit relaxation time $T_1 = 1/(\Gamma_- + \Gamma_+) = 1.6 \mu\text{s}$ for the excited state of the qubit and a Rabi decay time $T' = 1.6 \mu\text{s}$ [25]. From these measurements, the pure dephasing rate was estimated at $\gamma_\phi \equiv 1/T_\phi \approx 2 \times 10^5 \text{ s}^{-1}$. From qubit spectroscopy (see next section) an effective thermal bath temperature of $T = 120$ mK was determined, even though the mixing chamber of the dilution refrigerator was at 20 mK. At this effective temperature, $\kappa_+/\kappa_- \simeq \Gamma_+/\Gamma_- \simeq e^{-\hbar\omega_r/k_B T} \simeq 0.1$.

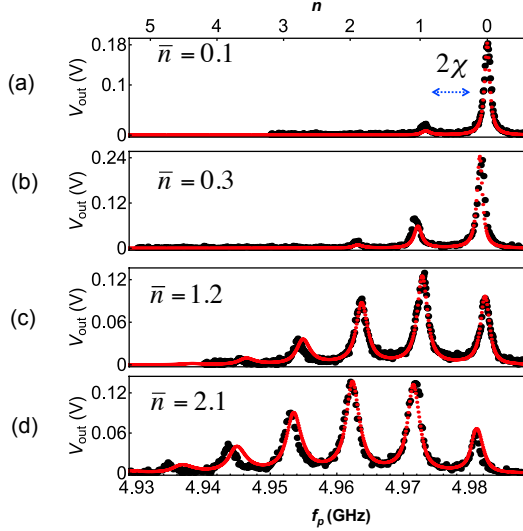


FIG. 4. (Color online) Photon number-splitting in the transmon spectrum. Black is data. Red is steady-state solution of the master equation Eq. 13. (a) Transmon spectrum with no coupler tone applied. The primary qubit transition is seen at $\tilde{\omega}_{ge}/2\pi = 4.982$ GHz. The peak at 4.973 GHz is due to a residual population of $n_{th} = 0.1$ photons in the resonator. (b) Spectrum when a coupler tone was applied at $\omega_c/2\pi = 5.474325$ GHz and power $P_{rf} = 2.5$ aW, producing a population of $\bar{n} = 0.3$ photons in the resonator. (c) Coupler tone of power $P_{rf} = 20$ aW, $\bar{n} = 1.2$ photons in the resonator. (d) Coupler tone of power $P_{rf} = 160$ aW, $\bar{n} = 2.1$ photons in the resonator.

V. DISCUSSION OF DATA AND COMPARISON WITH SIMULATION

When the resonator is weakly driven using a continuous coupler tone at the dressed resonant frequency $\tilde{\omega}_r - \chi$, we expect this to yield a coher-

ent state $|\alpha\rangle$ in the resonator such that $|\alpha|^2 = \bar{n}$ in the steady state (see Appendix A). The coherent state $|\alpha\rangle$ is a superposition of $|n\rangle$ states with a well-defined photon number n such that the probability w_n of seeing n photons obeys a Poisson distribution [27]. The qubit transition frequency is ac-Stark shifted (to lowest order in λ) by $\sim 2\chi n$ when the resonator is in the photon number-state $|n\rangle$. When $\chi \gg \Gamma$ (qubit line-width), individual peaks can be resolved in the qubit spectrum [4, 5], with the relative peak-heights obeying the Poisson distribution w_n . The average photon-number \bar{n} can then be calculated from the qubit spectrum using a number-weighted average as

$$\bar{n} = \frac{\sum_n w_n n}{\sum_n w_n}. \quad (14)$$

Figure 4(a) shows the transition spectrum of the transmon with no coupler tone applied to the resonator. The measured spectrum (black dots) shows a prominent peak at the qubit transition frequency of $\tilde{\omega}_{ge}/2\pi = 4.982$ GHz. The smaller spectroscopic peak, detuned by -9.3 MHz at $(\tilde{\omega}_{ge} + 2\chi)/2\pi = 4.973$ GHz, is due to one photon being present in the resonator. Assuming that this was from thermal excitations, we can use the relative heights of the two spectral peaks and Eq. 14 to estimate an equilibrium thermal population of $n_{th} = 0.10$ photons, corresponding to a temperature of about 120 mK for the resonator. We note that qubit spectroscopy close to the $|e\rangle \rightarrow |f\rangle$ transition frequency also revealed a small peak at $\omega_{ef}/2\pi$ (data not shown) consistent with a thermal population of the qubit with an effective temperature of 120 mK. This effective temperature is much higher than the 20 mK base temperature of the dilution refrigerator, possibly due to leakage of infrared photons [28] or insufficient cooling of an attenuator stage on the input or output microwave lines.

Figure 4(b) shows the measured transmon spectrum (black dots) when a weak coupler tone ($P_{rf} = 2.5$ aW) is applied at the resonant frequency $(\tilde{\omega}_r - \chi)/2\pi = 5.474325$ GHz of the dressed resonator. Here, an increase in the height of the $\tilde{\omega}_{ge} + 2\chi$ peak is observed and a

spectral peak at $\tilde{\omega}_{ge} + 4\chi$ appears. The $n = 0$ peak at $\tilde{\omega}_{ge}$ is still the largest. Figure 4(c) and (d) show the spectrum for an applied resonator drive power of 20 aW and 160 aW respectively. In this case, five or six spectral peaks are clearly observed. For $\bar{n} \gg n_{th}$, we found that the peak-heights obeyed a Poisson distribution [5, 6, 27], while for $n \approx n_{th}$ we observed significant discrepancy.

We also simulated the qubit spectrum using a steady-state solution of the master equation (Eq. 13). The red curves in Fig. 4 are the steady-state solutions to the master equation with different amplitudes of the coupler tone corresponding to those of the measured spectra (black). The parameters of the master equation were determined using independent spectroscopic and time-domain measurements as described in Sec. IV. Overall the simulation agrees well with the data. We note that in Fig. 4(d), the simulated spectrum deviates from data near the $n = 4$ and $n = 5$ photon peaks. This discrepancy probably occurred because the simulation did not include terms higher than the fourth order Kerr-type terms (see Eq. 11 and Eq. 13).

The average number of photons \bar{n} in the resonator was determined from each measured photon number-split spectrum using Eq. 14 [6]. Fig. 5 shows the average number of photons \bar{n} versus the applied power P_{rf} in attowatts (black '+' marks). For very weak driving $P_{rf} < 1$ aW, the thermal photon population $n_{th} = 0.1$ is the dominant contribution to \bar{n} . Above an applied power of $P_{rf} > 1$ aW, \bar{n} increases monotonically, but nonlinearly.

To understand this nonlinear dependence of \bar{n} on P_{rf} , we first consider using a semi-classical approach. Classically, we expect the mean occupancy of photons in the resonator to be given by

$$\bar{n} = 0.1 + \frac{P_{rf}/4\hbar Q_e}{\delta^2 + (\kappa_-/2)^2}, \quad (15)$$

where $\delta = \omega_c - (\tilde{\omega}_r - \chi)$ is the detuning of the coupler drive from the resonant frequency ($\tilde{\omega}_r - \chi$) [4, 6, 25]. The additional 0.1 accounts in an *ad hoc* way for the equilibrium thermal photon

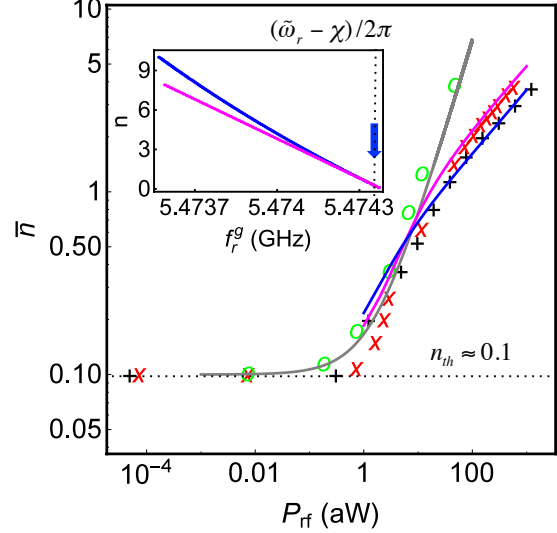


FIG. 5. (Color online) Average photon number \bar{n} in the resonator as a function of the applied microwave power P_{rf} . Black '+' marks show measured \bar{n} from weighted average of the qubit spectral peaks. Gray curve is the classical linear model (Eq. 16). Magenta curve is solution of the semiclassical nonlinear equation (Eq. 17) where a Kerr-type resonant frequency shift is included. Blue curve is the solution of the nonlinear equation (Eq. 18) where higher order nonlinearities are included through exact diagonalization. Red 'x' marks show \bar{n} computed from a weighted average of the spectra simulated using the system Master equation (Eq. 13) including the Kerr-type nonlinearities (up to fourth order in λ). Green circles show \bar{n} computed from weighted average of spectra simulated using the system master equation (Eq. 13) excluding Kerr nonlinearities. Inset shows shift of resonant frequency when the qubit is in $|g\rangle$ with increasing photon number calculated by including Kerr terms (magenta curve) from Eq. 6 and including higher-order nonlinearities through exact diagonalization of Eq. 1 (blue curve).

population n_{th} . In general, when δ is constant, the second term in Eq. 15 gives a linear relation between \bar{n} and P_{rf} . On resonance, $\delta = 0$ and Eq. 15 reduces to

$$\bar{n} = 0.1 + (Q_L/Q_e)P_{rf}/\kappa_- \hbar \omega_r. \quad (16)$$

The gray curve in the Fig. 5 shows the lin-

ear model given by Eq. 16. The experimental data deviates markedly from the linear model even at an average occupancy of one photon in the resonator. Note that the critical number of photons [19] for $g_{ge}/2\pi = 70$ MHz and $\Delta_{ge}/2\pi = -482$ MHz is $n_{crit} = \Delta_{ge}^2/4g_{ge}^2 \simeq 12$. Therefore, the deviation from linearity happens at $\bar{n} \ll n_{crit}$, as predicted by Gambetta *et al.* [4].

Although Eq. 16 is not well-obeyed over the full range of \bar{n} , the measured mean photon occupancy is nearly linear for $0.1 < \bar{n} < 0.5$. Using Eq. 16 and the measured \bar{n} from spectrum in Fig. 4(b), we find an attenuation of $\alpha = 65$ dB for the input microwave line. This estimate agrees reasonably well with the nominal attenuation of 60 dB (see Fig. 3).

The nonlinearity can be captured by realizing that $\delta(\bar{n})$ is in general a function of \bar{n} . As a first approximation, we include the shift in the resonant frequency only up to the Kerr-type terms (Eq. 6). This gives rise to the nonlinear equation

$$\bar{n} = 0.1 + \frac{P_{rf}/4\hbar Q_e}{\{(\zeta' - \zeta)\bar{n}\}^2 + (\kappa_-/2)^2}, \quad (17)$$

where the lowest order approximation $\delta = \omega_c - (\tilde{\omega}_r - \chi) \approx (\zeta' - \zeta)\bar{n}$ from Eq. 6 is used. The Kerr-type coefficients $\zeta/2\pi = 85$ kHz and $\zeta'/2\pi = -23$ kHz were estimated using Eq. 4 and Eq. 5. All of the parameters in Eq. 17 were determined from spectroscopy, allowing us to solve it in a self-consistent manner for \bar{n} with no fit parameters.

The magenta curve in Fig. 5 shows the solution of Eq. 17. We find that this qualitatively captures the nonlinear variation of \bar{n} with P_{rf} , and suggests that it arises due to the Kerr terms, which cause a change in the resonant frequency as \bar{n} is varied. The deviation from data for $\bar{n} > 0.5$ is possibly caused by ignoring terms of order higher than the Kerr terms.

We extended Eq. 17 to include higher order nonlinearities by writing

$$\bar{n} = 0.1 + \frac{P_{rf}/4\hbar Q_e}{[\delta(\bar{n})]^2 + (\kappa_-/2)^2}, \quad (18)$$

where the detuning $\delta(n) = \omega_c - \omega_r^g(n)$ was calculated from exact diagonalization of the generalized Jaynes-Cummings Hamiltonian (Eq. 1) with 10 transmon levels in the calculation. Equation 18 can be solved self-consistently to find the mean occupancy \bar{n} as a function of P_{rf} .

The solution of Eq. 18 is plotted as the blue curve in Fig. 5. We find that this agrees closely with the data, particularly in the $\bar{n} > 0.5$ range. This semiclassical model deviates from the data in the range $0.1 < \bar{n} < 0.5$, possibly due to the *ad hoc* nature in which the thermal photon population was included in Eq. 18.

The blue curve in the inset to Fig. 5 shows the calculated frequency of the resonator when the qubit is in the ground state ($f_r^g = \omega_r^g/2\pi$) as photon-number n in the resonator is varied, using an exact diagonalization of the generalized Jaynes-Cummings Hamiltonian (Eq. 1). The “bare” parameters of the Hamiltonian were determined from spectroscopic measurements (see Sec. III) and for the calculation, we used up to 10 transmon levels for greater accuracy. The magenta curve in the inset to Fig. 5 corresponds to the variation of f_r^g with n calculated using just the Kerr nonlinearity (Eq. 6).

We note that in the experiment, the coupler frequency is fixed at $\omega_c = \tilde{\omega}_r - \chi = 2\pi(5.474325)$ GHz (indicated by the blue arrow in the inset). The good agreement between the blue curve (solution to Eq. 18) and the data in Fig. 5 indicates that it is the change in the resonant frequency with \bar{n} that causes the nonlinear power-dependence of \bar{n} . Conversely, if the coupler frequency were adjusted to always drive on resonance, we expect \bar{n} would agree with the classical linear model (gray curve in Fig. 5).

For comparison, we also simulated the behaviour of the system using the full master equation (Eq. 13). The parameters used in the simulation were measured experimentally as discussed in Sec. IV. The red ‘x’ marks in Fig. 5 represent the average photon number computed by applying Eq. 14 to spectra numerically simulated using the master equation (Eq. 13) where the system Hamiltonian included terms up to the Kerr-type nonlinearities. As expected, \bar{n} calculated from the master equation solution

shows a nonlinear variation of \bar{n} with P_{rf} and it agrees closely with the semiclassical calculation which included up to the Kerr terms (magenta curve). We note that the \bar{n} from the master equation simulation shows a small but consistent deviation from the data (black ‘+’ marks) for $\bar{n} > 1$. This disagreement at higher power is likely due to contribution from higher order nonlinearities which have been ignored.

To verify that the Kerr terms cause the nonlinearity in \bar{n} , we set the Kerr terms to zero in the master equation simulation. The green circles in Fig. 5 show \bar{n} from this simulation, and the resulting curve falls near to the classical linear theory (gray curve) as \bar{n} increases.

Finally we note that the \bar{n} from master equation simulations (red ‘x’ marks and green circles) follow the data in the range of $0.1 < \bar{n} < 0.5$ more closely than the semiclassical simulations (blue and magenta). We believe this is because in our semiclassical analysis the thermal population $n_{th} = 0.1$ is included in a completely *ad hoc* manner. No such approximation was made in the master equation simulations. In general, at any non-zero temperature ($\kappa_+ \neq 0, \Gamma_+ \neq 0$), the probability distribution w_n is not Poissonian [5, 22]. A semiclassical model that better fits the data in the range $0.1 < \bar{n} < 0.5$, encompassing both coherent and thermal population of photons, is beyond the scope of this paper.

VI. CONCLUSION

In conclusion, we have measured a transmon coupled to a lumped-element resonator and observed a nonlinear dependence of the photon occupancy of the resonator \bar{n} versus the applied microwave power P_{rf} . The nonlinearity sets in at $\bar{n} \approx 1$, an order of magnitude smaller than the critical photon-number $n_{crit} \approx 12$ that determines the validity of the dispersive approximation. We found that the nonlinear dependence of \bar{n} on P_{rf} is caused by the fourth order (Kerr-type) terms in the system Hamiltonian. We compared our experimental results to numerical simulations of the system-bath master

equation in the steady state, as well as semiclassical models for a driven damped resonator and found good agreement when the variation of the resonant frequency with n is included.

Finally, we note that the high-fidelity read-out of the transmon state used in our experiment is based on the Jaynes-Cummings nonlinearity [14, 17, 21]. While this read-out allows single-shot measurements of the transmon state [14, 29, 30], the read-out fidelity ($\sim 80\%$) we typically achieve is much less than the fidelity of state preparation ($\sim 98\%$) [14]. The system master equation may be used to model this technique and quantitative understanding of the nonlinearities may lead to new or improved read-out techniques. For example, since this read-out depends on the strength of the Jaynes-Cummings interaction, the relative detuning between the qubit and resonator frequencies could play a role in the read-out fidelity [17] and study of this dependence may yield improvements in the read-out fidelity.

ACKNOWLEDGEMENTS

The authors would like to thank Rusko Ruskov for useful discussions. F. C. W. would like to acknowledge support from the Joint Quantum Institute and the State of Maryland through the Center for Nanophysics and Advanced Materials.

Appendix A: Coherent states as the solution of the driven damped oscillator

Here we review the steady state solutions of the master equation for a driven damped harmonic oscillator [27]. Ignoring the transmon, the master equation for a driven dissipative oscillator at $T = 0$ K is

$$\dot{\rho} = -\frac{i}{\hbar}[H_{osc}, \rho] + \kappa_- \mathcal{D}[a]\rho \quad (\text{A1})$$

where

$$H_{osc} = \hbar\omega_r a^\dagger a - \frac{\hbar\Omega_c}{2}(ae^{i\omega_c t} + a^\dagger e^{-i\omega_c t}) \quad (\text{A2})$$

and ω_r is the resonant frequency of the oscillator. The following equation can then be obtained from Eq. A1:

$$\begin{aligned} \frac{d\langle a^\dagger a \rangle}{dt} &= \frac{d\text{Tr}[\rho a^\dagger a]}{dt} = -\kappa_- \langle a^\dagger a \rangle \\ &+ \frac{i\Omega_c}{2} (\langle a^\dagger \rangle e^{-i\omega_c t} - \langle a \rangle e^{i\omega_c t}). \end{aligned} \quad (\text{A3})$$

Equation A3 confirms that photons decay from the resonator at a rate set by κ_- , in the absence of driving, *i.e.* $\Omega_c = 0$, and the resonator reaches the vacuum state $|0\rangle$ in steady state.

To show that the Glauber coherent states [27] are the steady state solutions of the master equation for the driven resonator, we first start with the Hamiltonian of the driven resonator:

$$H = \hbar\omega_r a^\dagger a - \frac{\hbar\Omega_c}{2} (a^\dagger e^{-i\omega_c t} + a e^{i\omega_c t}). \quad (\text{A4})$$

We then transform the Hamiltonian in Eq. A4 using the Glauber displacement operator $D^\dagger(\alpha)$ where

$$D(\alpha) = e^{\alpha a^\dagger - \alpha^* a}, \quad (\text{A5})$$

where α is a complex number characterizing the coherent state. Using

$$D^\dagger(\alpha) a^\dagger D(\alpha) = a^\dagger + \alpha^*, \quad (\text{A6})$$

the transformed Hamiltonian becomes:

$$\begin{aligned} \tilde{H} &= D^\dagger(\alpha) H D(\alpha) + i\hbar \frac{\partial D^\dagger(\alpha)}{\partial t} D(\alpha) \\ &= \hbar\omega_r a^\dagger a + \hbar a^\dagger [\omega_r \alpha - \frac{\Omega_c}{2} e^{-i\omega_c t} - i\dot{\alpha}] \\ &\quad + \hbar a [\omega_r \alpha^* - \frac{\Omega_c}{2} e^{i\omega_c t} + i\dot{\alpha}^*] \end{aligned} \quad (\text{A7})$$

The master equation Eq. A1 can also be transformed by $D^\dagger(\alpha)$ to read:

$$\begin{aligned} \dot{\rho} &= -\frac{i}{\hbar} [\tilde{H}, \rho] + \kappa_- \mathcal{D}[a]\rho \\ &\quad + \frac{\kappa_-}{2} (\alpha^* [a, \rho] - \alpha [a^\dagger, \rho]) \end{aligned} \quad (\text{A8})$$

Expanding \tilde{H} from Eq. A7, we have

$$\begin{aligned} \dot{\rho} &= -i\omega_r [a^\dagger a, \rho] + \kappa_- \mathcal{D}[a]\rho \\ &\quad - i[a^\dagger, \rho] \left(\omega_r \alpha - \frac{\Omega_c}{2} e^{-i\omega_c t} - i\dot{\alpha} - i\frac{\kappa_-}{2} \alpha \right) \\ &\quad - i[a, \rho] \left(\omega_r \alpha^* - \frac{\Omega_c}{2} e^{i\omega_c t} + i\dot{\alpha}^* + i\frac{\kappa_-}{2} \alpha^* \right). \end{aligned} \quad (\text{A9})$$

We are free to choose α such that the terms in the parentheses in Eq. A9 are zero, that is:

$$\omega_r \alpha - \frac{\Omega_c}{2} e^{-i\omega_c t} - i\dot{\alpha} - i\frac{\kappa_-}{2} \alpha = 0 \quad (\text{A10})$$

$$\omega_r \alpha^* - \frac{\Omega_c}{2} e^{i\omega_c t} + i\dot{\alpha}^* + i\frac{\kappa_-}{2} \alpha^* = 0 \quad (\text{A11})$$

Equations A10 and A11 are the same as the equations of motion of a classical oscillator [22]. With this choice of α , the transformed master equation Eq. A9 becomes simply

$$\dot{\rho} = -i\omega_r [a^\dagger a, \rho] + \kappa_- \mathcal{D}[a]\rho \quad (\text{A12})$$

which is nothing but the master equation for an undriven oscillator, *i.e.* Eq. A1 with $\Omega_c = 0$.

We already noted that the steady state solution for the undriven oscillator is the ground state or vacuum state $|0\rangle$. However to arrive at Eq. A12 we began by transforming the Hamiltonian H using the displacement operator $D^\dagger(\alpha)$. If the untransformed steady state solution is $|\psi_{ss}\rangle$, then we can write

$$D^\dagger(\alpha) |\psi_{ss}\rangle = |0\rangle \quad (\text{A13})$$

Noting that $D^\dagger(\alpha) = D(-\alpha)$, we find

$$|\psi_{ss}\rangle = D(\alpha) |0\rangle = |\alpha\rangle, \quad (\text{A14})$$

where $|\alpha\rangle$ is a Glauber coherent state [27]. Thus a damped oscillator at $T = 0$ K that is initially in the ground state $|0\rangle$ goes into a coherent state $|\alpha\rangle$ under harmonic driving, where α satisfies the classical equation of motion Eq. A10. Note that at a non-zero temperature, the distribution of Fock-states becomes thermal, while α satisfies the classical oscillator equations [22].

Considering the coupled transmon-resonator system, we note that up to second order in the

dispersive approximation ($\chi\sigma_z(a^\dagger a)$), the only effect the qubit has on the resonator is to shift the resonant frequency. In this case the above analysis can be applied, since the resonator

is still linear. We note that in the presence of higher-order nonlinearities, the Glauber displacement transformation of the master equation is non-trivial.

-
- [1] J. Koch, T. M. Yu, J. Gambetta, A. A. Houck, D. I. Schuster, J. Majer, A. Blais, M. H. Devoret, S. M. Girvin, R. J. Schoelkopf, *Phys. Rev. A* **76**, 042319 (2007).
 - [2] A. Wallraff, D. I. Schuster, A. Blais, L. Frunzio, R.-S. Huang, J. Majer, S. Kumar, S. M. Girvin, R. J. Schoelkopf, *Nature* **431**, 162 (2004).
 - [3] A. Wallraff, D. I. Schuster, A. Blais, J. M. Gambetta, J. Schreier, L. Frunzio, M. H. Devoret, S. M. Girvin, R. J. Schoelkopf, *Phys. Rev. Lett.* **99**, 50501 (2007).
 - [4] J. Gambetta, A. Blais, D. I. Schuster, A. Wallraff, L. Frunzio, J. Majer, M. H. Devoret, S. M. Girvin, R. J. Schoelkopf, *Phys. Rev. A* **74**, 042318 (2006).
 - [5] D. I. Schuster, A. A. Houck, J. A. Schreier, A. Wallraff, J. M. Gambetta, A. Blais, L. Frunzio, J. Majer, B. Johnson, M. H. Devoret, S. M. Girvin, R. J. Schoelkopf, *Nature* **445**, 515 (2007).
 - [6] B. Suri, Z. K. Keane, R. Ruskov, Lev S. Bishop, C. Tahan, S. Novikov, J. E. Robinson, F. C. Wellstood, B. S. Palmer, *New J. Phys.* **15**, 125007 (2013).
 - [7] A. A. Houck, D. I. Schuster, J. M. Gambetta, J. A. Schreier, B. R. Johnson, J. M. Chow, L. Frunzio, J. Majer, M. H. Devoret, S. M. Girvin, R. J. Schoelkopf, *Nature* **449**, 328 (2007).
 - [8] I. -C. Hoi, T. Palomaki, J. Lindkvist, G. Johansson, P. Delsing, C. M. Wilson *Phys. Rev. Lett.* **108**, 263601 (2012).
 - [9] G. Kirchmair, Z. Leghtas, S. E. Nigg, Hanhee Paik, E. Ginossar, M. Mirrahimi, L. Frunzio, S. M. Girvin, R. J. Schoelkopf, *Nature* **495**, 205 (2013).
 - [10] B. Vlastakis, G. Kirchmair, Z. Leghtas, S. Nigg, L. Frunzio, S. M. Girvin, M. Mirrahimi, R. J. Schoelkopf, *Nature* **342**, 607 (2013).
 - [11] I. -C. Hoi, C. M. Wilson, G. Johansson, T. Palomaki, B. Peropadre, P. Delsing, *Phys. Rev. Lett.* **107**, 073601 (2011).
 - [12] S. Novikov, J. E. Robinson, Z. K. Keane, B. Suri, F. C. Wellstood, B. S. Palmer, *Phys. Rev. B* **88**, 060503(R) (2013).
 - [13] I. Siddiqi, R. Vijay, F. Pierre, C. M. Wilson, M. Metcalfe, C. Rigetti, L. Frunzio, M. H. Devoret, *Phys. Rev. Lett.* **93**, 20 (2004).
 - [14] M. D. Reed, L. DiCarlo, B. R. Johnson, L. Sun, D. I. Schuster, L. Frunzio, R. J. Schoelkopf, *Phys. Rev. Lett.*, **105**, 173601 (2010).
 - [15] N. Bergeal, R. Vijay, V. E. Manucharyan, I. Siddiqi, R. J. Schoelkopf, S. M. Girvin, M. H. Devoret, *Nat. Phys.*, **6**, 296 (2010).
 - [16] M. Hartridge, R. Vijay, D. H. Slichter, J. Clarke, I. Siddiqi, *Phys. Rev. B*, **83**, 134501 (2011).
 - [17] M. Boissonneault, J. M. Gambetta, A. Blais, *Phys. Rev. Lett.* **105**, 100504 (2010).
 - [18] E. T. Jaynes, F. W. Cummings, *Proc. IEEE* **51**, 89 (1963).
 - [19] A. Blais, R. -S. Huang, A. Wallraff, S. M. Girvin, R. J. Schoelkopf, *Phys. Rev. A* **69**, 062320 (2004).
 - [20] P. Carbonaro, G. Compagno, F. Persico, *Phys. Lett. A* **73**, 97 (1979).
 - [21] Lev S. Bishop, E. Ginossar, S. M. Girvin, *Phys. Rev. Lett.* **105**, 100505 (2010).
 - [22] E. Thuneberg, “Quantum Optics in Electric Circuits”, Lecture Notes, Dept. of Physics, Univ. of Oulu (2013).
 - [23] A. Einstein, *Z. Phys* (1917).
 - [24] Z. Kim, B. Suri, V. Zaretskey, S. Novikov, K. D. Osborn, A. Mizel, F. C. Wellstood, B. S. Palmer, *Phys. Rev. Lett.* **106**, 120501 (2011).
 - [25] B. Suri, “Transmon qubits coupled to superconducting lumped element resonators”, Ph. D. Thesis, Dept. of Physics, Univ. of Maryland, College Park (2015).
 - [26] G. J. Dolan, *App. Phys. Lett.* **31**, 337 (1977).
 - [27] R. J. Glauber, *Phys. Rev.* **131**, 2766 (1963).
 - [28] A. D. Córcoles, J. M. Chow, J. M. Gambetta, C. Rigetti, J. R. Rozen, G. A. Keefe, M. B. Rothwell, M. B. Ketchen, M. Steffen, *Appl. Phys. Lett.* **99**, 181906(2011).
 - [29] Hanhee Paik, D. I. Schuster, Lev S. Bishop, G. Kirchmair, G. Catelani, A. P. Sears, B. R. Johnson, M. J. Reagor, L. Frunzio, L. I. Glazman, S. M. Girvin, M. H. Devoret, R.

- J. Schoelkopf, *Phys. Rev. Lett.* **107**, 240501 (2011).
- [30] J. M. Chow, J. M. Gambetta, A. Córcoles, S. T. Merkel, J. A. Smolin, C. Rigetti, S. Poletto, G. A. Keefe, M. B. Rothwell, J. R. Rozen, M. B. Ketchen, M. Steffen, *Phys. Rev. Lett.* **109**, 060501 (2012).